ACID-TREATED CLAY MINERALS AS CATALYSTS FOR DEHYDRATION OF METHANOL AND ETHANOL

Monika Marosz, Andrzej Kowalczyk, Barbara Gil, and Lucjan Chmielarz*

[1]Faculty of Chemistry, Jagiellonian University, Gronostajowa 2, 30-387 Kraków, Poland

Abstract—The purification of clay minerals prior to their use as catalysts can escalate processing costs so methods are needed whereby less purification is necessary. One such potential method is acid treatment of the unpurified clay minerals. The main objectives of the present study were to develop the optimal acid-treatment conditions and to determine how the acidic properties of the modified clay samples influenced their catalytic capability toward the dehydration of ethanol and methanol. Clay mineral samples – allophane, palygorskite, and sepiolite, without purification – were acid treated (0.8 M HNO_3; 95°C; 2, 8, or 24 h) and after calcination (500°C; 6 h) tested as catalysts for the conversion of methanol to dimethyl ether and of ethanol to diethyl ether and ethene. The changes in chemical and structural compositions as well as surface acidity of the mineral samples were analyzed and correlated with their catalytic performance. Among the samples studied, allophane was the most catalytically active in the dehydration of methanol to dimethyl ether. Acid treatment of this mineral sample decreased methanol conversion slightly. An opposite effect was found for ethanol dehydration to diethyl ether, where acid treatment increased catalytic activity of allophane. The differences in catalytic performance of the mineral samples were discussed with respect to the nature and concentration of acid sites.

Keywords—Alcohol dehydration · Allophane · Catalysis · Palygorskite · Sepiolite

INTRODUCTION

Clay minerals, due to their very large variety of structures, textures, and chemical compositions, as well as, in many cases, abundance in nature, are very promising materials for various applications, including catalysis. An important advantage of minerals is the possibility of modifying them by various methods and, therefore, tailoring their properties for specific applications (Galarneau et al. 1995; Chmielarz et al. 2012; Marosz et al. 2019). An example is the intercalation of clay minerals with metal polyoxocations by ion-exchange, followed by their calcination, resulting in pillared interlayered clays (PILCs) (Chmielarz et al. 2004, 2011; Mnasri-Ghnimi and Frini-Srasra 2019). Other examples are porous clay heterostructures (PCHs) obtained by intercalation of clay minerals with silica (or silica doped with selected metal oxide species) pillars by the surfactant directed method (Galarneau et al. 1995; Chmielarz et al. 2018). Intercalation of clay minerals with inorganic pillars results in the opening of their interlayer space and, therefore, formation of porous materials with a relatively large specific surface area and porosity, especially in the case of PCHs. These properties are very important for the possible catalytic applications of such modified minerals. The main drawbacks of the clay intercalation methods are their relatively high cost as well as problems with their scale-up and the reproducibility of the catalyst's production. The catalytic functionalization of minerals has been studied mainly for pure or purified mineral samples at the laboratory scale. The scaling-up of such processes to the industrial scale is difficult (for various reasons, not least the need for purification of the raw material) and limits application of minerals as industrial catalysts. Therefore, in the present studies the mineral samples, without additional purification but modified by

simple thermal and acid treatments, were tested as potential catalysts for methanol and ethanol dehydration. These modifications can be relatively easily transformed from laboratory to much larger scale and, therefore, the costs of catalyst production can be reduced significantly.

Dimethyl ether (DME) and diethyl ether (DEE) are the main products of the low-temperature dehydration of methanol and ethanol, respectively. The DME and DEE syntheses from alcohols are known to be acid-catalyzed and exothermic reactions. Typical commercial catalysts used for the methanol-to-DME (MTD) process are solid acid materials, such as $\gamma\text{-}Al_2O_3$, zeolites, silica-alumina, and phosphorus-alumina (Abu-Dahrieh et al. 2012; Alamolhoda et al. 2012; Rownaghi et al. 2012). In the case of ethanol dehydration, because of thermodynamic restrictions, DEE is the main reaction product in the low-temperature range, while at higher temperatures mainly ethene is produced. Also in this process, the solid acid materials, such as $\gamma\text{-}Al_2O_3$, zeolites, and modified clay minerals (Srinivasan et al. 2019; Batchu et al. 2019; Marosz et al. 2019), were reported to be effective catalysts. Thus, the acidic properties of the catalysts are critical in both reactions and determine their catalytic efficiency. The role of the nature of the acid sites and strength in the catalytic conversion of alcohols is, however, still a topic of discussion. In a previous paper (Marosz et al. 2019), the greater catalytic activity of strong acid sites present in modified clay minerals was reported in the reactions of methanol and ethanol dehydration. On the other hand, Zheng et al. (2011) reported a very important role of the nature of the acid sites in the zeolitic catalysts. Both Lewis and Lewis ratio. In the case of the acid-treated acid sites were reported to be active in the MTD process; however, greater catalytic efficiency of the Lewis ratio. In the case of the acid-treated acid was suggested. Thus, discussion related to the role of acid sites and the possible

reaction mechanisms are still under debate (Zheng et al. 2011; Marosz et al. 2019).

The products of methanol and ethanol dehydration are very important chemicals for the chemical and petrochemical industries. DME is one of the most promising, environmentally friendly, and economic diesel fuel additives, and possibly also as an alternative fuel for future applications (Rownaghi et al. 2012). DME has a high cetane number of ~55–60, which shows its potential as diesel fuel and as a fuel additive (Yaripour et al. 2005; Abu-Dahrieh et al. 2012; Rownaghi et al. 2012). Moreover, a lack of C–C bonds in DME molecules limits the formation of carbon soot during fuel combustion, which is a typical problem of diesel engines. DME is also commonly used as a key intermediate for the production of important chemicals, such as dimethyl sulfate or methyl acetate, as well as a source of hydrogen for fuel cells and fuel in gas turbines (Yaripour et al. 2005; Stiefel et al. 2011; Rownaghi et al. 2012). Due to properties similar to propane and butane, DME can be used as a liquified petroleum gas (LPG) substitute in domestic and industrial energy supply (Yaripour et al. 2005; Stiefel et al. 2011; Rownaghi et al. 2012; Tokay et al. 2012).

For thermodynamic reasons, the dehydration of ethanol results mainly in the formation of DEE at lower temperatures, while at higher temperatures ethene becomes the main reaction product. DEE is characterized by a cetane number >125 and, therefore, has excellent properties for transportation fuels (Varisli et al. 2007; Takahara et al. 2015). These properties make DEE a promising alternative fuel or diesel fuel additive (Kito-Borsa et al. 1998). Blending of DEE with ethanol was reported to improve the cold-start problem in ethanol-fueled cars (Ciftci et al. 2012). The second product of ethanol dehydration, ethene, is a main feed stock for the chemical and petrochemical industries.

Allophane, palygorskite, sepiolite, and their acid-treated forms apparently have not been tested as potential catalysts for these conversion reactions. Such minerals contain acid sites of medium strength, which are potential active sites for dehydration of alcohols. Moreover, using such relatively easily available minerals as well as cheap methods of catalytic activation should result in the development of catalytic materials with a promising potential for future industrial applications. The aim of the present study was, therefore, to measure the catalytic performance of natural allophane, palygorskite, and seipolite, without purification or modification other than by acid and thermal treatment, in the dehydration and conversion of alcohols to ethers.

EXPERIMENTAL

Preparation of Catalysts

Minerals allophane (Allo/Ab), palygorskite (Plg), and sepiolite (Sep), supplied by S&B Industrial Minerals GmbH (Marl, Germany), were used as raw materials (without any purification) for the preparation of catalysts for dehydration of alcohols. Raw minerals (10 g) were dispersed in a solution of 0.8 M nitric acid (100 mL; POCh,

Gliwice, Poland) and stirred at 95°C for 2, 8, or 24 h. Then the samples were separated by filtration, washed with distilled water, and dried at 80°C. Finally, the samples were calcined at 500°C for 6 h. The samples obtained were denoted as X-2, X-8, and X-24, where X (A, P, or S) corresponds to the type of mineral used and numbers (2, 8, or 24) to duration (h) of the acid treatment. The samples marked as X-0 were not acid activated but were calcined at 500°C for 6 h.

Characterization of Catalysts

The chemical compositions of the samples were determined by inductively coupled plasma-optical emission spectroscopy (ICP-OES) using an iCAP 7400 instrument (Thermo Scientific, Bedford, Massachusetts, USA). The solid samples were dissolved in a mixture of hydrofluoric, sulfuric, and phosphoric acid solution assisted by microwave radiation using an Ethos Easy system (Milestone, Sorisole, Italy). All chemicals used for the mineral dissolution were of traceselect quality (for ultratrace analysis) and were supplied by Fluka (Munich, Germany). The X-ray diffraction (XRD) patterns of the samples were obtained using a D2 PHASER powder diffractometer (Bruker, Billerica, Massachusetts, USA). The measurements were taken using CuKα radiation (λ = 1.54184 Å) in the range 3–70°2θ with a step of 0.02°2θ and a counting time of 1 s per step. The Fourier-transform infrared (FTIR) spectra of the samples were recorded on a Spectrum 100 spectrometer (Perkin-Elmer, Shelton, Connecticut, USA) equipped with a ZnSe crystal detector (attenuated total reflectance, ATR, technique). Spectra were collected over 100 scans in the range of 4000–525 cm^{-1} with a resolution of 4 cm^{-1}. The ultraviolet-visible-diffuse reflectance (UV-Vis-DR) spectra of the samples were obtained with an Evolution 600 spectrophotometer (Thermo Scientific, Bedford, Massachusetts, USA). The measurements were performed in the range of 190–900 nm with a resolution of 2 nm. Textural parameters of the samples were determined by N$_2$ adsorption-desorption measurements at −196°C using an ASAP 2010 (Micromeritics, Norcross, Georgia, USA) instrument. Prior to the measurements, the samples were outgassed under vacuum at 350°C for 24 h. The specific surface area values were determined using the Brunauer-Emmett-Teller (BET) equation. The total pore volume was determined by means of the total amount of adsorbed nitrogen at a relative pressure (p/p_0) of 0.98.

Surface acidity of the samples was analyzed by temperature-programmed desorption of ammonia (NH$_3$-TPD) and analysis of the samples adsorbed with pyridine by FTIR. NH$_3$-TPD measurements were carried out in a flow microreactor system equipped with a QMS detector (PREVAC, Rogów, Poland). Before the experiments, the samples were outgassed in a flow of pure helium at 500°C for 1 h. The ammonia sorption was carried out at 70°C in a flow of gas mixture containing 1.0 vol.% of ammonia diluted in helium (total flow rate of 20 mL/min). The

desorption process was carried out under controlled temperature conditions (linear heating rate of 10°C/min) in a flow of pure helium (20 mL/min). The contribution of Brønsted (BAS) and Lewis (LAS) acid sites was investigated by FTIR spectroscopy based on the adsorption of pyridine as the probe molecule. The samples, in the form of self-supporting wafers, were thermally activated at 450°C for 1 h prior to the adsorption of pyridine at 170°C. All spectra recorded in absorbance mode were normalized to the standard 10 mg pellet (density 3.2 mg/cm^2). The concentrations of LAS and BAS sites were estimated using previously reported absorption coefficients (Gil et al. 2014): $\varepsilon(LAS) = 0.165$ cm^2/µmol, $\varepsilon(BAS) = 0.044$ cm^2/µmol, and the intensities of the corresponding pyridine maxima (1545 cm^{-1} for BAS and ~1445 cm^{-1} for LAS) after pyridine desorption at 170°C to ensure complete removal of weakly adsorbed species.

Catalytic Tests

Methanol and ethanol dehydration processes were carried out under atmospheric pressure in a flow fixed-bed quartz microreactor packed with 0.1 g of the catalyst. Before the catalytic test, the sample was outgassed in a flow of pure helium at 500°C for 30 min. The gas mixture containing alcohol (3.9 vol.% of methanol or 3.3 vol.% of ethanol) diluted in helium was introduced into the reactor (isothermal saturator at 0°C, flow rate of 20 mL/min). The amount of alcohols in the reaction mixtures was related to the volatility of these alcohol vapors at a saturation temperature of 0°C. The measurements were carried out in the temperature range 100–350°C with isothermal steps every 25°C. The reaction temperature was measured by a K-type thermocouple placed inside the microreactor in the catalyst bed. The reaction mixture, after passing the microreactor, was analyzed by a gas chromatograph SRI 8610C (SRI Instruments, Torrance, California, USA) equipped with a HayeSep D column as well as a methanizer and FID detector. The operating temperature of the chromatography column was 120°C or 180°C in the case of methanol and ethanol dehydration, respectively. For each isothermal step three chromatographic analyses were performed and averaged.

RESULTS

A solution of HNO$_3$ instead of the often used hydrochloric acid (Vicente-Rodriguez et al. 1996; Ayodele and Abdullah 2019) was employed for acid treatment of the mineral samples. Treatment of the samples with mineral acids results in the modification of their chemical compositions as well as structural and textural properties, but also results in deposition of residual amounts of NO$_3^-$ or Cl$^-$ anions in the case of treatment with the solutions of HNO$_3$ or HCl, respectively. Chloride compounds are known to poison various catalytic systems (Tian et al. 2019) and, therefore, application of nitric acid is much better for the preparation of catalysts. Moreover, NO$_3^-$ anions are decomposed to O$_2$ and nitrogen oxides during the calcination process of the acid-treated mineral samples. A calcination

temperature of 500°C is high enough to decompose thermally any NO$_3^-$ anions present in the clay samples (Madarász et al. 2007; Mironyuk et al. 2016). The same acid-treatment conditions were used to compare the efficiency of this process for each mineral sample. The different durations of the acid treatment were important for optimization of the catalytic activation of the mineral samples.

XRD, FTIR, and UV-Vis-DR Analyses of Allophane

XRD (Fig. 1a)   As a typical short-range ordered aluminosilicate, the XRD pattern of allophane exhibits two major broad reflections in the 19–32 and 34–43°2θ ranges (Opiso et al. 2009; Kaufhold et al. 2010). The former reflection is related to an interference between neighboring silicon tetrahedra (Du et al. 2018) and is similar to the reflection of synthetic silica gel. The latter reflection is also related to the short-range ordering and is very sensitive to the thermal treatment of allophane (Du et al. 2018). Moreover, the presence of well crystalized albite with the allophane was proved by the characteristic reflections at 22.8, 24.5, 28.1, 28.7, 33.1, 35.6, and 48.4°2θ (Xu et al. 2017). Furthermore, the reflections characteristic of illite (10.6, 14.0, 27.7, 28.7, 30.4, 31.6, 34.7, and 42.6°2θ) (Rastsvetaeva et al. 2009), quartz (20.9, 26.7, 35.9, 39.5, 50.2, and 60.1°2θ) (Ikuta et al. 2007), and cristobalite (23.8 and 31.6° 2θ) (Pluth et al. 1985) were identified in the XRD pattern of this allophane sample (Fig. 1A). The main change observed in the sample treated at 500°C (sample A-0) was decreased intensity of the reflections characteristic of allophane. A similar effect of thermal treatment of allophane was reported by other researchers (Kitagawa 1974; Du et al. 2018) and was explained as being due to dehydroxylation, which probably changes the coordination of Al^{3+} from octahedral to tetrahedral (Kitagawa 1974) and induces the formation of poorly ordered material. No significant changes in intensity of the reflections characteristic of other mineral components were observed, which suggests their relatively high thermal stability. Treatment of the Allo/Ab (mixture of allophane and albite) sample with a solution of nitric acid followed by calcination at 500°C resulted in a significant weakening of the reflections characteristic of allophane, which is related to the extraction of Al cations from this mineral (Table 1) and, therefore, destruction of its structure. This Al leaching may also have been responsible for the decrease in intensity of the reflections characteristic of albite and illite. Quartz and cristobalite are much more stable in acidic media; a significant reduction in intensity of the characteristic reflections was observed for these minerals, however. Note that acid treatment resulted mainly in the extraction of Al from the mineral sample. Moreover, Fe was partially removed from the mineral sample, however, and the efficiency of iron leaching was significantly less than that of Al. Other components were not leached from the mineral structure in significant amounts (Table 1). The most significant changes in the chemical composition of the Allo/Ab sample occurred during the first 2 h of acid treatment. For the prolonged acid activation from 2 to 8 or 24 h the changes in chemical composition were less significant. Apparently, during the first 2 h the components less stable in acidic conditions were leached, while the removal of the more
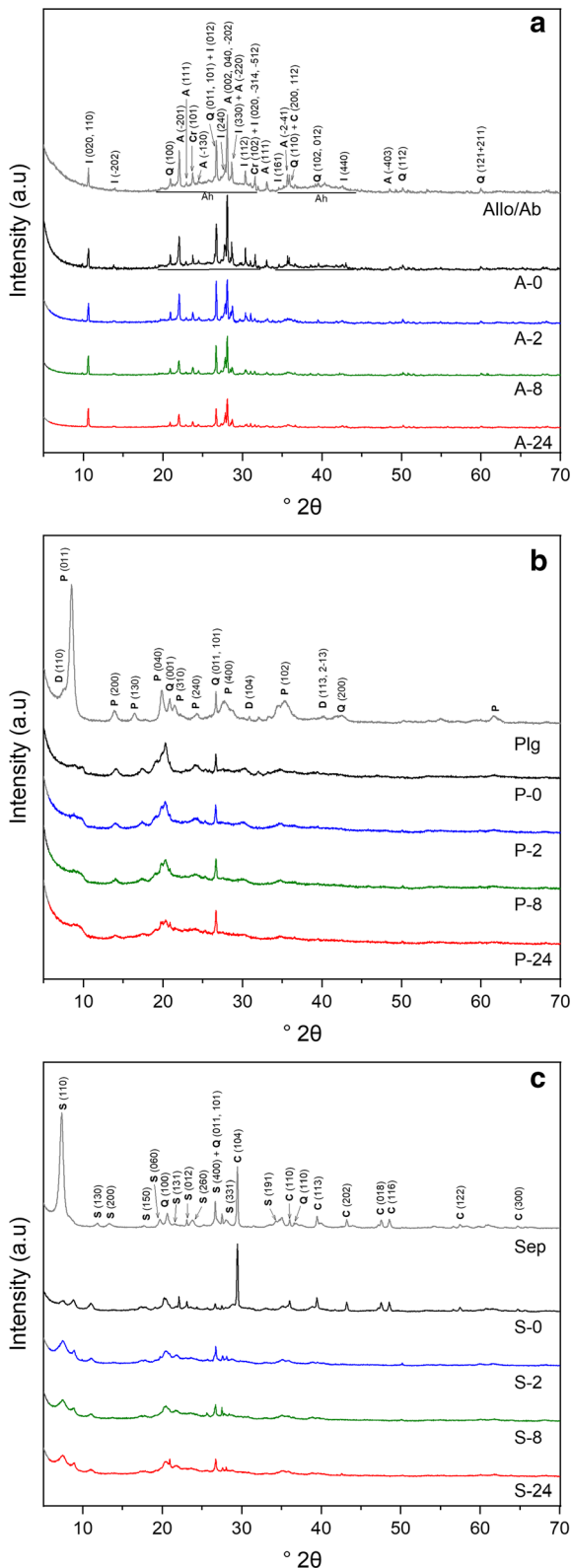
Fig. 1. XRD patterns of the untreated and acid-treated forms of **a** allophane, **b** palygorskite, and **c** sepiolite. Q: Quartz, Cr: Cristobalite, I: Illite, A: Albite, Ah: Allophane, P: Palygorskite, D: Dolomite, S: Sepiolite, C: Calcite

stable components was also less effective in the prolonged acid treatment procedure.

FTIR Spectroscopy (Fig. 2a)   For the raw Allo/Ab sample three main bands at ~990, 920, and 550 cm^{-1}, characteristic of allophane, were detected (Pérez et al. 2016; Thill 2016). The former two bands are assigned to the Si-O stretching vibrations, and the third to the Al-O-Si deformation vibrations (Rampe et al. 2012; Du et al. 2018). The shoulder at ~1135 cm^{-1} is assigned to the in-plane Si-O stretching vibrations (Du et al. 2018). The weak band at ~1485 cm^{-1} corresponds to the O_3–Si–OH vibrations (Pérez et al. 2016). Moreover, the band at ~1635 cm^{-1} is assigned to the O-H deformations, while the shoulder at ~680 cm^{-1} is assigned to the O-H out-of-plane bending vibrations in H_2O (Pérez et al. 2016). The broad band at ~3300 cm^{-1} is related to the vibrations of –OH groups interacting with water molecules by Van der Waals forces (Chmielarz et al. 2010). Bands located in the range 770–800 cm^{-1} are related to the presence of quartz and possibly also cristobalite (Bosch Reig et al. 2002). The most significant changes observed in the spectrum of the sample treated at 500°C (A-0) were related to the decreased intensity or even disappearance of the bands assigned to allophane at 990, 920, and 550 cm^{-1}. Moreover, the band at ~990 cm^{-1} was shifted slightly toward higher frequencies, which could be explained by the condensation of silica tetrahedra and the formation of more disordered Al–O bonds following the dehydroxylation of Si-OH and breakdown of Si–O–Al bonds (Du et al. 2018). Dehydroxylation of silanols is also proved by a decrease in intensity of the bands at ~3300, 1635, and 680 cm^{-1}, related to the presence of adsorbed water molecules. Thus, the results of the FTIR and XRD analyses are consistent with each other and show thermal degradation of allophane.

Treatment of the Allo/Ab sample with nitric acid resulted in a shift of the band from 1000 to ~1025 cm^{-1} due to a gradual condensation of silica, while a new shoulder at ~620 cm^{-1} was assigned possibly to the Al-O-Al vibrations, suggesting the formation of small disordered alumina oxide aggregates (Colomban 1989; Ue et al. 1997). Aluminum cations were partially leached from the mineral samples during acid treatment. Such cations possibly formed small aggregated species in the solution, which were re-deposited on the mineral sample surface.

UV-Vis-DR (Fig. 3)   The spectrum recorded for Allo/Ab consisted of three bands located at ~240, 350, and 485 nm (Fig. 3a). Among the elements identified by chemical analysis in this sample, absorption of radiation in the UV-Vis range occurred only for iron and titanium species. The molar content of iron is ~ten times greater than that of titanium (Table 1). Thus, the bands present in the spectrum are related mainly to the different forms of iron in the mineral sample. The band at ~240 nm is attributed to iron cations in tetrahedral coordination (Bailly et al. 2005), possibly as inclusions in the structure of allophane and albite. Some of the Si^{4+} and Al^{3+} in the tetrahedral sheet of illite were probably substituted by iron cations.

Table 1. Chemical composition (wt.) of raw and acid-modified minerals

Sample	SiO$_2$	Al$_2$O$_3$	Fe$_2$O$_3$	CaO	MgO	Na$_2$O	K$_2$O	TiO$_2$
A-0	56.70	25.07	9.16	2.80	3.14	1.49	0.57	1.08
A-2	63.86	15.85	8.89	3.40	4.41	1.77	0.72	1.10
A-8	65.03	14.98	8.64	3.48	4.31	1.84	0.70	1.04
A-24	66.67	13.18	8.29	3.35	4.26	1.70	0.61	0.92
P-0	68.95	11.58	4.44	1.98	10.93	0.88	0.75	0.49
P-2	73.12	11.15	4.50	0.16	9.78	0.05	0.64	0.57
P-8	74.85	10.69	3.93	0.15	9.11	0.05	0.66	0.55
P-24	78.39	8.99	3.62	0.16	7.62	0.04	0.61	0.57
S-0	63.00	3.21	0.98	13.13	18.62	0.28	0.63	0.13
S-2	81.33	3.28	1.19	0.24	12.91	0.20	0.69	0.17
S-8	81.09	3.65	1.40	0.32	12.38	0.22	0.75	0.19
S-24	82.72	3.57	1.28	0.36	10.98	0.21	0.71	0.17

The shoulder on the right side of this band is related to the presence of iron cations in octahedral coordination, possibly in the octahedral sheet of illite (Bailly et al. 2005; Kowalczyk et al. 2017). The band at ~350 nm is related to iron oligomeric (FeO)$_n$ species, while that at ~485 nm is assigned to small Fe$_2$O$_3$ crystallites (Boroń et al. 2019). Because reflections characteristic of Fe$_2$O$_3$ were not found in the XRD patterns, the size of these crystallites is thought to be below the XRD detection limit. Thermal treatment of Allo/Ab at 500°C (A-0) resulted in a small decrease in intensity of the band related to monomeric iron cations and an increase in the bands assigned to aggregated species. Acid treatment resulted in no significant changes in the spectra of the A-2, A-8, and A-24 samples.

XRD, FTIR, and UV-Vis-DR Analyses of Palygorskite

XRD (Fig. 1b)   In the XRD pattern for palygorskite the characteristic reflections at 8.5, 13.9, 16.3, 19.8, 21.5, 24.3, 27.7, 35.4, and 61.7°2θ were identified (dos Santos Soares et al. 2013). Reflections characteristic of quartz (20.8 and 42.5°2θ) and dolomite (30.9 and 40.2°2θ) were also found (Effenberger et al. 1981; Ikuta et al. 2007). Thermal treatment of the Plg sample (P-0) resulted in the disappearance of the reflection at 8.5°2θ and the appearance of two weak reflections at 8.7 and 9.8°2θ, which were considered to be due to the formation of palygorskite anhydrite. Other reflections characteristic of palygorskite were significantly reduced or even disappeared. In addition, the weak reflection, appearing at 30.1°2θ in the P-0 XRD pattern, implied the formation of amorphous silica. Magnesium was partially removed from the palygorskite framework. Similar results were reported by Li et al. (2017).

Acid treatment of the Plg sample resulted in a gradual decrease in intensity of the reflections characteristic of palygorskite, showing a progressive degradation of its structure. Moreover, acid treatment resulted in a significant decrease in calcium, magnesium, and sodium contents (Table 1), which is related to the decomposition of dolomite and possibly also sodium carbonate in acidic conditions. The most significant changes in calcium, magnesium, and sodium contents were observed during the first 2 h of acid treatment, thus dolomite and sodium carbonate impurities were possibly decomposed in the initial stage of the acid-treatment procedure. Aluminum leaching by acid treatment was also observed, but it was significantly less intense than that of the Allo/Ab sample (Table 1).

FTIR (Fig. 2b)   The most intense bands characteristic of palygorskite at ~970, 1010, and 1190 cm^{-1} are assigned to the stretching vibration of the Si–O bond (Papoulis et al. 2010). The bands at ~910 and 880 cm^{-1} are related to the deformation vibrations of Al(OH)Al and Al(OH)Fe, respectively, while the weak band at ~1455 cm^{-1} corresponds to the O$_3$–Si–OH vibrations (Madejová & Komadel 2001; Pérez et al. 2016). Further, the band at ~1650 cm^{-1} is assigned to the O-H deformation, and the shoulder at ~660 cm^{-1} is assigned to the O-H out-of-plane bending vibrations in H$_2$O (Madejová & Komadel 2001; Pérez et al. 2016). The bands characteristic of the O–H stretching of the structural hydroxyl groups and OH stretching of water molecules coordinated to Al^{3+} or Mg^{2+} cations are at ~3610 and 3540 cm^{-1}, respectively. The band at ~660 cm^{-1} is assigned to the O-H out-of-plane bending vibrations in H$_2$O (Pérez et al. 2016), and the broad band at ~3350 cm^{-1} is related to the vibrations of O-H groups interacting with water molecules by Van der Waals forces (Chmielarz et al. 2010). The bands present in the range 770–800 cm^{-1} are related to quartz and possibly also cristobalite (Bosch Reig et al. 2002).

Thermal treatment of palygorskite (P-0) resulted in a disappearance of or decrease in bands related to adsorbed water (3540, 3350, 1650, and 660 cm^{-1}) and O-H groups (3610 and
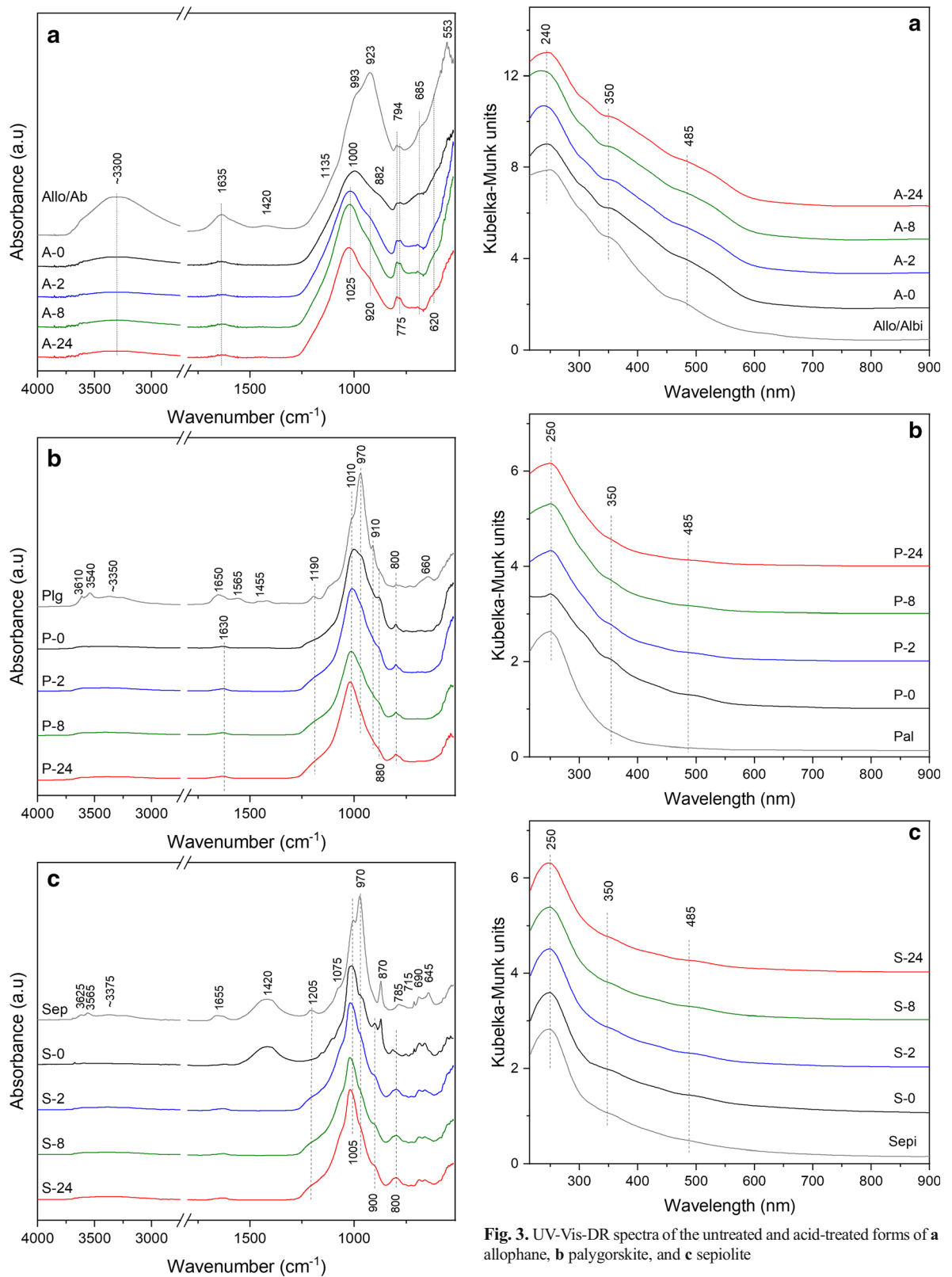
Fig. 2. ATR-FTIR spectra of the untreated and acid-treated forms of **a** allophane, **b** palygorskite, and **c** sepiolite

Fig. 3. UV-Vis-DR spectra of the untreated and acid-treated forms of **a** allophane, **b** palygorskite, and **c** sepiolite

910 cm^{-1}), indicating dehydration and partial dehydroxylation of the sample. The decrease in intensity of the band at ~970 cm^{-1} suggests the partial decomposition of the Plg structure, possibly with the formation of amorphous silica aggregates. The new, weak band at ~1630 cm^{-1} may be due to water molecules adsorbed on the amorphous silica surface (Vinoda et al. 2015).

Acid treatment of Plg resulted only in a slight modification of its spectrum. The main differences were related to the increased intensity of the band characteristic of the Al(OH)Fe deformation vibrations at ~880 cm^{-1}, which may be the result of partial leaching of aluminum and iron from the mineral and the formation of new species (e.g. precipitation of Al- and Fe-species).

UV-Vis-DR (Fig. 3b) Among elements identified in the samples (Table 1) only for iron and titanium species is adsorption of radiation in the UV-Vis range possible. The molar ratio of iron to titanium was in the range 6.5–8, so the bands in the spectra must be mainly from iron species. The intensive band at ~250 nm is a superposition of two sub-bands assigned to iron ions in tetrahedral and octahedral sites (Bailly et al. 2005). Thermal treatment of raw palygorskite resulted in the formation of new weak bands at ~350 and 485 nm assigned to small iron oxide oligomeric (FeO)$_n$ species and small Fe$_2$O$_3$ crystallites, respectively (Boroń et al. 2019). Acid treatment of Plg resulted in a gradual decrease in intensity of the bands related to these forms of iron, suggesting that extraction of iron from such species in acidic media is more effective than that of iron cations from the mineral framework.

XRD, FTIR, and UV-Vis-DR Analyses of Sepiolite

XRD (Fig. 1c) Reflections characteristic of sepiolite occur at ~7.3, 11.7, 13.4, 17.7, 19.6, 21.6, 23.0, 23.7, 26.7, 28.1, and 34.2°2θ (Liu et al. 2018a, b). Moreover, the reflections characteristic of calcite at 29.4, 36.0, 39.5, 43.1, 47.5, 48.6, 57.4, and 64.8°2θ (Liu et al. 2018a) as well as quartz at 20.5 and 26.7°2θ (Effenberger et al. 1981) were identified, and led to the conclusion that sepiolite is the main component of the mineral sample, while calcite and quartz were also present as mineral impurities. Thermal treatment of the sample at 500°C (S-0) resulted in a decrease in intensity of the reflections characteristic of sepiolite, especially distinct for the reflection at ~7.3°2θ. Moreover, two new reflections appeared at ~8.7 and 11.0°2θ. A similar effect was observed by Perraki & Orfanoudaki (2008), who attributed such changes in the XRD pattern to dehydration of sepiolite with the formation of sepiolite anhydrite. Acid treatment of Sep (S-2, S-8, and S-24) resulted in decomposition of calcite, manifested by the disappearance of the reflections characteristic of this phase. Decomposition of calcite occurred during the first 2 h of acid treatment. Acid treatment of the Sep sample resulted in a significant decrease in calcium content (Table 1), which was related to dissolution of calcite. Moreover, a decrease in magnesium content, observed for the acid-treated samples, suggests that small amounts of dolomite might be present in the raw sepiolite sample. In contrast to the previous mineral samples, the changes in the amounts of aluminum and iron in Sep and its modifications were very small (Table 1). Thus, cations of these elements are very stable in the sepiolite structure. The most significant changes in the chemical composition of the sepiolite sample occurred during the first 2 h of acid treatment, thus calcite and dolomite impurities were possibly decomposed during the initial stage of the acid-treatment procedure.

FTIR (Fig. 2c) The intense bands characteristic of sepiolite and assigned to the Si–O stretching vibrations, are located at ~1005, 1075, and 1205 cm^{-1} (Frost et al. 1998, 2009). Moreover, the OH deformation vibrations, characteristic of the sepiolite structure, are present at ~715, 785, and 970 cm^{-1}, while at 690 and 645 cm^{-1} the bands characteristic of the OH translation vibration occur (Frost et al. 1998, 2009). The band characteristic of the O–H stretching of water molecules coordinated to Mg^{2+} cations is at ~3625 cm^{-1}, while at ~3565 cm^{-1} the band assigned to the O–H stretching vibrations in coordinated water molecules occur (Pérez et al. 2016). Moreover, the broad band at ~3375 cm^{-1} is related to the vibrations of O-H groups interacting with water molecules by Van der Waals forces (Chmielarz et al. 2010). The bands characteristic of calcite, present at ~870 and 1420 cm^{-1}, are assigned to the CO$_3^{2-}$ asymmetric vibrations (Rodriguez-Blanco et al. 2011). Thermal treatment of raw sepiolite at 500°C (S-0) resulted in a decrease or even disappearance of the bands related to adsorbed water and also the structural O-H groups, indicating dehydration and also partial dehydroxylation of the sample. Acid treatment of Sep resulted in the disappearance of the bands characteristic of calcite. Calcite was decomposed during the first 2 h of acid treatment (S-2), in agreement with the results of XRD studies.

UV-Vis-DR (Fig. 3c) Analysis of the chemical composition of the mineral samples, (Table 1), shows that among elements identified in the samples, only iron and titanium species adsorb radiation in the UV-Vis range. Because the molar ratio of iron to titanium in the samples of this series is >6.0 the bands in the spectra are assigned mainly to the presence of iron species. The intense band located in the spectrum of raw sepiolite at ~250 nm is related to iron ions in both tetrahedral and octahedral coordinations (Bailly et al. 2005). Moreover, weak bands at ~350 and 485 nm are related to small iron oxide oligomeric (FeO)$_n$ species and small Fe$_2$O$_3$ crystallites, respectively (Boroń et al. 2019). Neither thermal nor acid treatment of raw sepiolite resulted in significant changes in the spectra, indicating the stability of iron species present in the mineral sample.

Texture and Surface Acidity

The textural parameters of the samples were analyzed by low-temperature dinitrogen adsorption and desorption (Fig. 4), while surface acidity was determined by NH$_3$-TPD and FTIR analysis of samples adsorbed with pyridine (Table 2).

N_2 Adsorption/desorption

The isotherms of a series of the Allo/Ab samples were characterized by an increase in adsorbed volume at very low relative pressure, indicating significant microporosity. The gradual increase in the adsorbed volume of N_2 with increasing relative pressure was assigned to the well developed external surface of the samples. Micropores in such samples were probably located between aggregated particles of allophane (Du et al. 2018). The hysteresis loop belongs to type H4, which is commonly associated with aggregated particles (Thommes et al. 2015). Acid treatment for 2 h resulted in a significant decrease of the BET surface area from 184 to 129 m^2/g, while extending the acid treatment to 8 or 24 h yielded 143 and 171 m^2/g, respectively. A similar tendency was found for changes in pore volume. This interesting effect may be the result of parallel processes of leaching of components from the mineral into solution and partial precipitation of these components or their deposition onto the mineral surface, which may have blocked some of the pore entrances.

The isotherms of the palygorskite samples (Fig. 4B) belong to type IV (IUPAC classification) and indicated the presence of both meso- and micropores (Sing et al. 1985; Sing & Williams 2004). Acid treatment of the raw palygorskite (P-0) resulted in an increase in N_2 adsorbed volume in the range characteristic of capillary condensation

in micropores. Thus, acid treatment of palygorskite resulted mainly in development of microporosity. The BET surface area
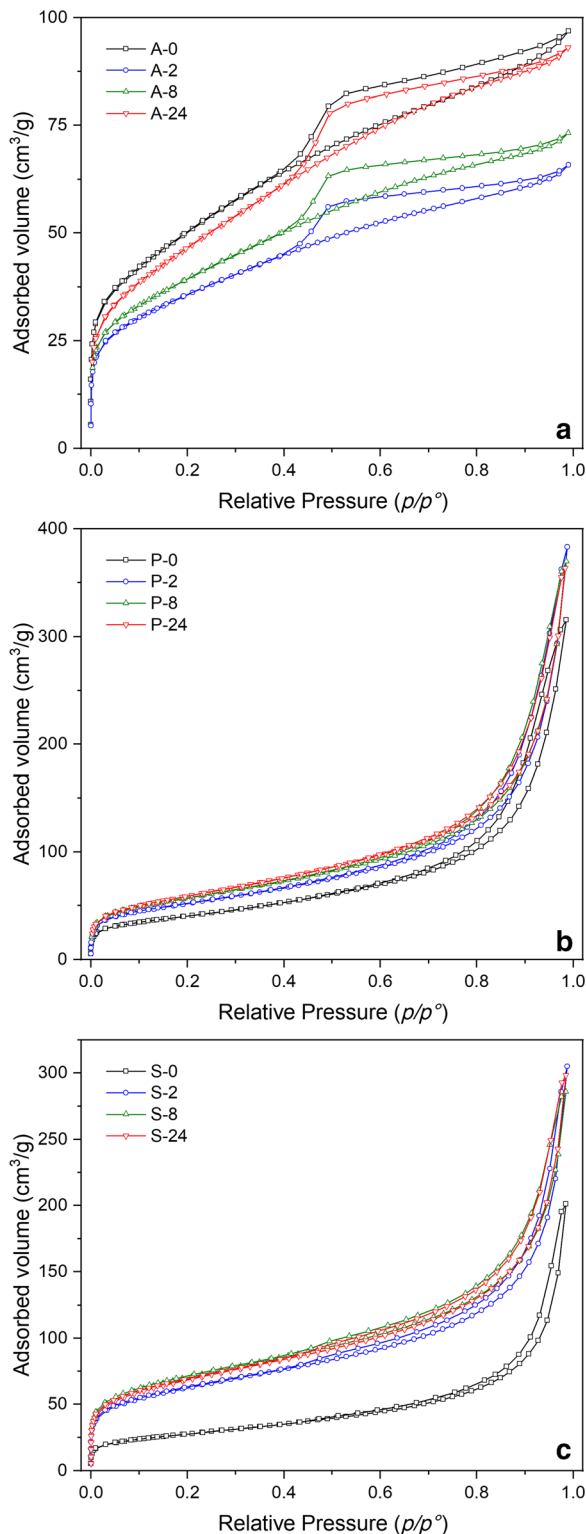

Fig. 4. Nitrogen adsorption-desorption isotherms of the untreated and acid-treated forms of **a** allophane, **b** palygorskite, and **c** sepiolite

Table 2. Textural parameters and surface acidity of raw and acid-modified minerals

Sample	S_{BET} (m^2/g)	V_{total} (cm^3/g)	SA (μmol/g)	DA ($\mu mol/m^2$)	Brønsted /Lewis[*] (%/%)
A-0	184	0.150	267	1.456	19/81
A-2	129	0.102	128	0.999	25/75
A-8	143	0.113	136	0.952	24/76
A-24	171	0.144	143	0.836	24/76
P-0	144	0.489	97	0.672	15/85
P-2	186	0.594	161	0.866	16/84
P-8	205	0.573	168	0.820	16/84
P-24	213	0.563	171	0.803	17/83
S-0	99	0.311	49	0.500	-[**]
S-2	223	0.472	156	0.698	7/93
S-8	253	0.442	148	0.584	9/91
S-24	247	0.462	155	0.628	12/88

SA – surface acidity (number of acid sites in 1 g of the sample)

DA – surface density of acid sites (number of acid sites on 1 m^2 surface of the sample)

*the contribution of Brønsted and Lewis acid sites was determined by FTIR analysis of the samples adsorbed with pyridine, after outgassing at 170°C.

**the molar ratio of Brønsted /Lewis was not determined due to overlapping of bands characteristic of carbonates and adsorbed pyridine.

increased from 144 m^2/g for P-0 to 213 m^2/g for P-24 (Table 2). The most significant increase in pore volume was observed in the sample treated with acid solution for 2 h (P-2), while 8 and 24 h treatments resulted in a decrease in pore volume. This effect may be caused by the competitive processes of Al^{3+}, Mg^{2+}, and Fe^{3+} extraction, their precipitation in the solution, and finally, re-deposition on the surface of the mineral sample.

Dinitrogen adsorption-desorption isotherms obtained for the calcined sepiolite sample (S-0) and its acid-treated forms (S-2, S-8, and S-24) (Fig. 4C), belong to the type IV (IUPAC classification), indicating the presence of both meso- and micropores (Sing et al. 1985; Sing & Williams 2004). Similar to palygorskite, acid treatment of Sep resulted in an increase in N$_2$ adsorbed volume in the range characteristic of the capillary condensation in micropores. For the Sep samples this effect is much more distinct than for the Plg series. Thus, also in this case, acid treatment of the mineral sample resulted mainly in development of microporosity. The specific surface area increased more than twice after 2 h of acid treatment, from 99 to 223 m^2/g (Table 2). The extension of the acid treatment duration from 2 to 8 and 24 h resulted in less significant additional increases in S_{BET} of S-8 and S-24.

NH$_3$-TPD

The NH$_3$-TPD profile obtained for the calcined Allo/Ab sample (A-0) consisted of two broad and overlapping peaks centered at ~170 and 285°C, attributed to desorption of ammonia from weaker and stronger acid sites, respectively (Fig. 5a). The surface acidity was derived mainly from aluminum and iron cations on the mineral surface. Acid treatment of the Allo/Ab sample resulted in a significant decrease in intensity of ammonia desorption profiles as well as surface concentration and density of acid sites (Table 2). For the samples treated with nitric acid (A-2, A-8, and A-24), the surface acidity decreased by ~40–50%, depending on the duration of acid treatment (Table 2), which was the result of leaching of aluminum cations. More than one third of the aluminum was removed from the Allo/Ab sample during the first 2 h of acid treatment (Table 1). Extending acid treatment from 2 to 8 and 24 h resulted in less effective leaching of aluminum. Analysis of the nature of acid sites in the A-0 sample showed that ~19% of them were of Brønsted type and ~81% of Lewis type (Table 2). Acid treatment resulted in an increased contribution of the Brønsted type (23–25%) and decreased contribution of the Lewis type (75–77%) acid sites.

Desorption of ammonia from the surface of the calcined palygorskite (P-0) was manifested by the broad desorption maxima centered at ~200 and 370°C (Fig. 5b), due to ammonia chemisorbed on weaker and stronger acid sites, respectively. Treatment of the raw palygorskite sample resulted in a significant increase in intensity of these maxima. The most significant increase in the surface concentration and density of acid sites were observed during the first 2 h of acid treatment (P-2). Extending the duration of this acid treatment (P-8 and P-24) failed to yield any significant increase in these properties (Table 2). The effect of the increased surface acidity of the
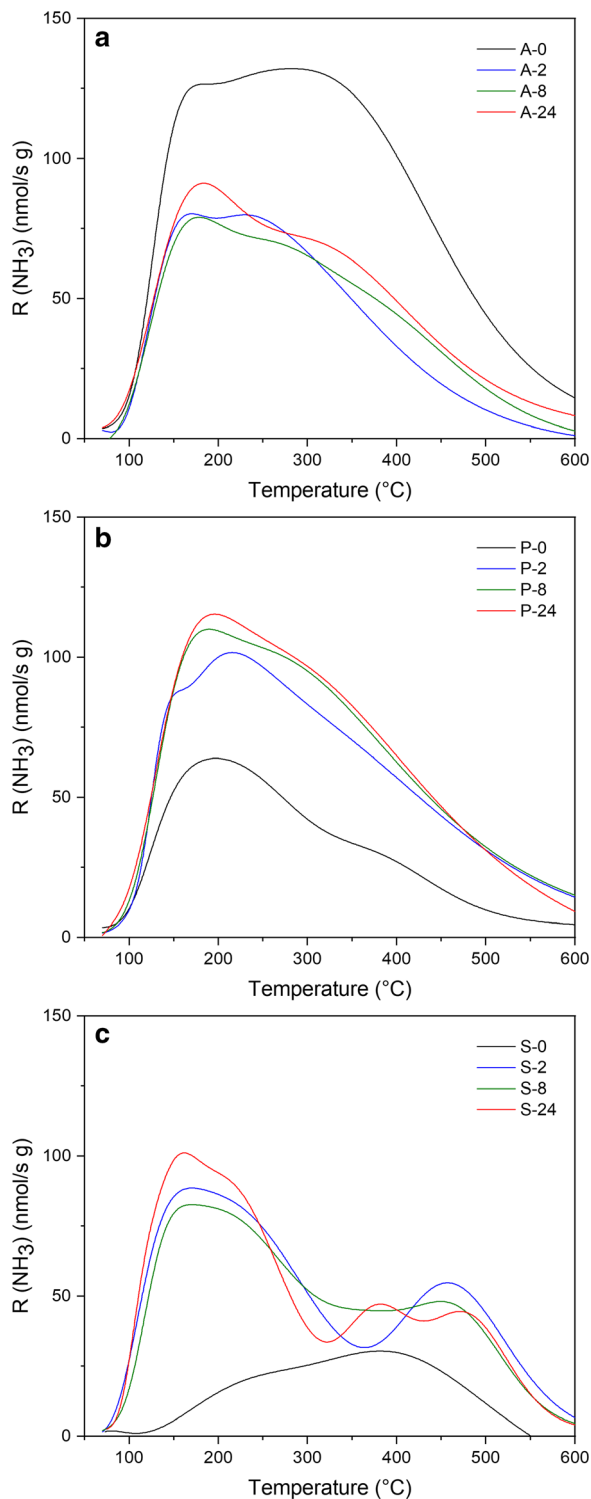

Fig. 5. NH$_3$-TPD profiles of the untreated and acid-treated forms of **a** allophane, **b** palygorskite, and **c** sepiolite

samples was possibly related to the partial leaching of octahedral cations (Al^{3+}, Mg^{2+}, and possibly also Fe^{3+}) and their

partial precipitation in the solution with the formation of metal hydroxide-oxide aggregates and/or re-deposition on the palygorskite surface. Such modifications resulted in the movement of Al^{3+}, and possibly also of Fe^{3+}, from structural positions inaccessible or scarcely accessible to positions easily accessible to ammonia and also other molecules, thus creating an acidic interface. The analysis of the nature of acid sites in P-0 showed that ~15% were Brønsted type and 85% Lewis type (Table 2). Acid treatment resulted in a slight increase in the Brønsted type (16–18%) and decreased the Lewis type (82–84%). A decrease in aluminum content in the Plg series of the acid-treated samples was less significant, however, than in the Allo/Ab series (Table 1), which is due to the greater stability of aluminum cations in palygorskite.

The ammonia desorption profile obtained for the calcined sepiolite sample (S-0) was characterized by at least two broad and unresolved maxima centered at ~220 and 380°C (Fig. 5c). Acid treatment of the Sep sample for 2 h (S-2) split these bands into an intense maximum from the relatively weak acid sites at ~170°C and a weaker maximum at ~450°C from the much stronger acid sites. The surface concentration of acid sites increased by more than three times, from 49 to 156 μmol/g (Table 2). Such significant changes in the desorption profiles and surface concentrations of acid sites observed for S-0 and S-2 are attributed to the decomposition of basic calcite ($CaCO_3$) during acid treatment of the raw mineral sample. Acid treatment not only removed the basic components, but also significantly developed its specific BET surface area and porosity (Table 2). Moreover, an increase in the surface concentration of acid sites is also associated with the competitive processes of extraction of Mg^{2+}, Al^{3+}, and Fe^{3+} cations from the octahedral sheets of sepiolite, as well as their partial precipitation and/or re-deposition on the sepiolite surface. As in the case of palygorskite, such modification placed these components in positions more accessible by ammonia and other molecules. Assuming that Al^{3+} and Fe^{3+} were re-deposited on the mineral

surface and were responsible for the formation of acid sites, the surface acidity of such acid-treated samples would increase significantly. The ammonia desorption profiles of other acid-treated samples of this series were similar to those of S-2; however, in the case of S-8, the overlapping of the low- and high-temperature maxima was greater. In the case of the S-24 sample a new peak located at ~380°C, related to acid sites of medium strength, appeared. The relative contributions of Brønsted sites was significantly lower (7–12%) and the Lewis sites dominated (88–93%).

Catalytic Performance

Thermally and acid-treated mineral samples were tested as catalysts for dehydration of methanol to dimethyl ether (DME) as well as dehydration of ethanol to diethyl ether (DEE) and ethene. In both these reactions the surface acidity of the catalyst played a crucial role (Macina et al. 2016; Chmielarz et al. 2018).

Allophane

The results obtained for the methanol dehydration reaction (Fig. 6a) revealed for the series of Allo/Ab samples a very good catalytic activity; however, the greatest conversion of methanol and selectivity for DME was obtained from the thermally treated sample (A-0). The methanol conversion increased greatly at ~300°C, reaching ~83%; at higher temperatures, methanol conversion was significantly less. This effect is related to the thermodynamic limitations, as the dehydration of methanol is a slightly exothermic reaction. An increase in the reaction temperature shifted the enthalpy of reaction to higher values and, therefore, the reaction equilibrium was reduced (Diep & Wainwright 1987). A decrease in the selectivity for DME, observed at higher reaction temperatures, was due to the formation of formaldehyde, carbon monoxide, and methane, which were side reaction products. For A-0, the selectivities for these side products at 350°C were ~11.0, 0.4, and 0.01% for formaldehyde, carbon monoxide, and methane, respectively.
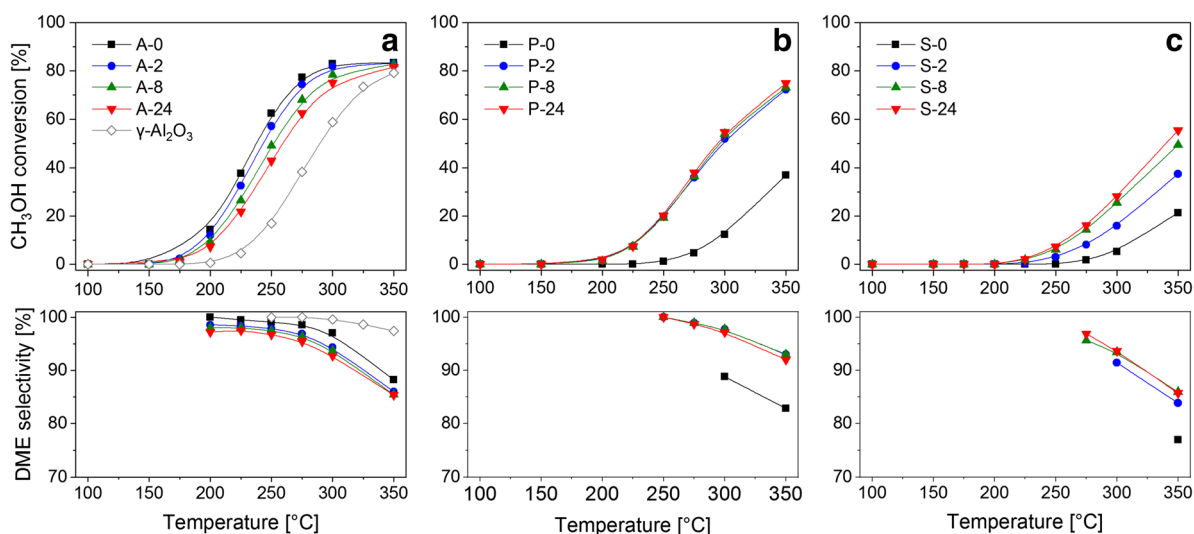

Fig. 6. Temperature dependence of methanol conversion and DME selectivity in the process of methanol dehydration over **a** allophane-, **b** palygorskite-, and **c** sepiolite-based catalysts

Acid treatment of the Allo/Ab sample gradually decreased both its catalytic activity and selectivity for DME. This is not surprising, taking into account that the crucial parameter determining catalytic activity is the surface acidity of the samples. Acid treatment decreased the Al content (Tables 1 and 2) and, therefore, reduced the surface concentration of acid sites. The selectivity for the side reaction products was reduced by nearly twice as much for the acid-treated samples compared to sample A-0. For comparison, the results of the catalytic tests for γ-Al$_2$O$_3$, which is one of the commercial catalysts used for methanol to DME conversion, were obtained (Fig. 6a) and these revealed that the Allo/Ab based catalysts, especially A-0, exhibited much better catalytic performance than γ-Al$_2$O$_3$, indicating that Allo/Ab is very promising for future commercial applications.

Palygorskite

The efficiency of the methanol to DME dehydration reaction in the presence of the thermally treated palygorskite sample (P-0) (Fig. 6b) was rather poor. A significant contribution of the side reaction products was detected for this catalyst at higher reaction temperatures (at 350°C ~12% of formaldehyde, 4.7% of methane, and 0.1% of CO). Acid treatment, however, significantly increased the catalytic activity of this mineral sample and decreased its selectivity for the side reaction products. Methanol conversions in this case were still significantly less than for the Allo/Ab series.

Comparing surface concentrations of acid sites (Table 2) and results from catalytic tests demonstrated that in the acid-treated palygorskite samples (P-2, P-8, P-24) the surface concentration of acid sites was greater than in the acid-treated Allo/Ab samples (A-2, A-8, A-24). The hypothesis that only surface concentration and strength of acid sites in the catalysts determine catalytic performance would have predicted the opposite; so this hypothesis is rejected. Instead, a new hypothesis was formulated, that the nature of acid sites, i.e. Brønsted vs Lewis, is also very important. In the case of the Allo/Ab series, more Brønsted acid sites were produced than in the palygorskite series. For the most active Allo/Ab samples (A-0), the Brønsted fraction of acid sites was ~19% (Table 2), which, taking into account the large surface concentration of acid sites (267 μmol/g), amounted to ~50 μmol/g of Brønsted sites. Acid treatment decreased slightly the estimated concentrations of Brønsted acid sites to 32, 33, and 34 μmol/g for A-2, A-8, and A-24, respectively, which may also explain the slight decrease in catalytic activity (Fig. 6).

For the Plg series, the estimated concentrations of Brønsted acid sites were much lower – 15, 26, 27, and 29 μmol/g for P-0, P-2, P-8, and P-24, respectively. Thus, the catalytic activity of the Plg series was less than that for the Allo/Ab series.

Sepiolite

Calcined sepiolite (S-0) yielded the lowest activity toward methanol dehydration to DME and the highest selectivity for the side reaction products (at 350°C ~17% of formaldehyde, 6.7% of methane, and 0.2% of CO) among all the studied mineral samples (Fig. 6C). This is not surprising because this sample is characterized by the lowest concentration of acid sites (Table 2). Acid-treatment of the sepiolite sample not only increased the content of surface acid sites, but also modified their distribution with respect to different strengths (Fig. 5c). The ammonia desorption profiles were split into two ranges, low- and high-temperature, indicating ammonia desorbing from weaker and stronger acid sites, respectively. The maximal methanol conversion for this series was obtained by S-24 (56% at 350°C), but was significantly lower than the acid-treated samples of the other series. The selectivity for DME was less than for the modified palygorskite samples and very similar to that obtained in the Allo/Ab series. The estimated amount of Brønsted acid sites in the sepiolite series was 11, 13, and 19 mmol/g for S-2, S-8, and S-24, respectively, which correlates with their relatively low catalytic activity.

DISCUSSION

Comparison of the catalytic performances of Allo/Ab, Plg, and Sep sample series leads to the conclusion that the best catalytic properties in the reaction of methanol dehydration to DME are given by the calcined Allo/Ab sample, which was attributed to the large surface concentration of Brønsted acid sites. Similar results were reported by Zheng et al. (2011) who studied a series of zeolite composites with hierarchical porous structures and tunable acidities. A correlation with the Brønsted/Lewis ratio and DME selectivity, as well as methanol conversion, in the MTD process over such zeolitic catalysts was shown. The methanol conversion increased linearly, while the DME selectivity decreased with an increase in the Brønsted/Lewis ratio. In the case of the acid-treated Allo/Ab samples, the Brønsted/Lewis ratio was greater than that of A-0 but the total surface concentration of acid sites, including the Brønsted sites, was significantly less than for A-0 . Thus, the decrease in the catalytic activity of the acid-treated Allo/Ab samples may have been related to the lower surface concentration of the Brønsted acid sites.

Palygorskite and sepiolite were significantly less catalytically active in the process of methanol to DME conversion. The results of the catalytic dehydration of ethanol revealed that diethyl ether (DEE) and ethene were the main reaction products (Fig. 7). Due to thermodynamic restrictions, DEE was produced at lower temperatures, while ethene was the main reaction product at elevated temperatures. Moreover, at higher temperatures, the formation of acetaldehyde, the main side-reaction product, and smaller amounts of carbon monoxide, methane, ethane, and C$_3$ hydrocarbons were observed. The conversion of ethanol was significantly more successful than the conversion of methanol for all the studied catalysts. Among them the best ethanol conversions were obtained for the series of Allo/Ab samples. In this case the ethanol conversion started at ~150°C and reached 99% at 350°C.

In contrast to methanol dehydration, acid treatment of the Allo/Ab sample resulted in a small increase in ethanol conversion. This effect may be related to the intense conversion of ethanol to ethene, which dominated at higher reaction temperatures. The mechanism for this process may include the direct
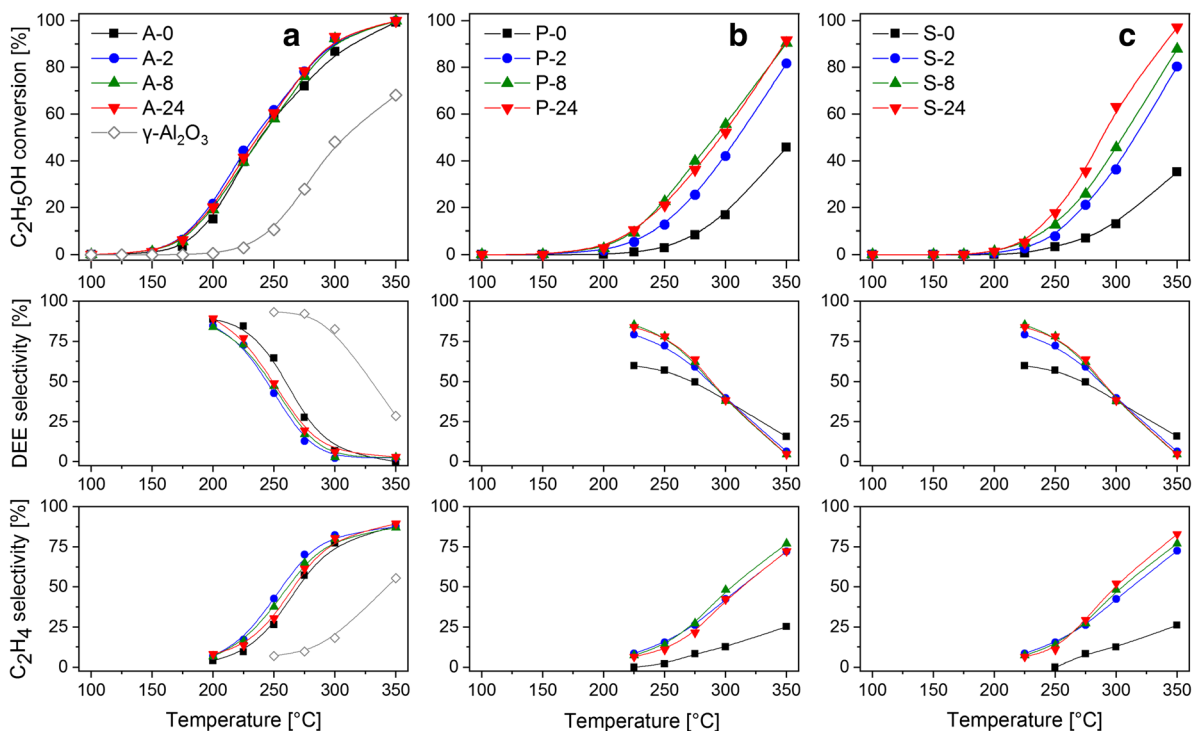
Fig. 7. Temperature function of ethanol conversion and DEE and ethylene selectivity in the process of ethanol dehydration over **a** allophane-, **b** palygorskite-, and **c** sepiolite-based catalysts

interaction of the hydroxyl group of ethanol with the Brønsted acid site, resulting in the formation of the surface ethoxide species and evolution of water molecules. In the next step the Lewis base site is necessary to eliminate protons from surface ethoxide resulting in the formation of ethene (Kondo et al. 2005; Barthos et al. 2006). Thus, in the case of ethanol-to-ethene conversion not only Brønsted acid sites but also Lewis base sites are necessary. The differences in the catalytic activity within the Allo/Ab series apparently were related to variable amounts of Lewis base sites. Further studies are need to explain this interesting effect.

DEE was the main reaction product at lower temperatures, but an increase in the reaction temperature resulted in increased selectivity towards ethene and a decrease in the selectivity for DEE, which agrees with the thermodynamic restrictions mentioned earlier. The important role of the Brønsted acid site is assigned to the conversion of ethanol to DEE (Kondo et al. 2005; Barthos et al. 2006). The formation of side-reaction products was intensified at higher temperatures, e.g. for A-24 at 350°C the formation of acetaldehyde (9.8%), ethane (0.01%), methane (0.06%), and carbon monoxide (0.02%) was detected.

The series of palygorskite-based catalysts exhibited lower catalytic activity in the reaction of ethanol to DEE dehydration (Fig. 7b) compared to the Allo/Ab catalysts. Acid treatment significantly increased their catalytic activity, though ethanol conversions in this case were lower than for the Allo/Ab series. The selectivity for DEE was higher, while the selectivity for ethene was lower than for the Allo/Ab catalysts. The formation

of the side products at higher reaction temperatures was greater than for the Allo/Ab series, e.g. for P-24 at 350°C the formation of acetaldehyde (21.0%), ethane (0.01%), methane (0.01%), carbon monoxide (0.01%), and C_3 hydrocarbons (0.01%) was detected.

Calcined sepiolite (S-0) had the lowest catalytic activity of all the mineral samples studied; however, acid modification significantly increased its catalytic activity (Fig. 7c). For the most active catalyst of this series (S-24), ethanol conversion was obtained at 350°C and the extent of conversion was similar to that of the acid treated Allo/Ab catalysts. Thus, in this case, acid treatment resulted in effective catalytic activation of the mineral sample. The selectivity for DEE and ethene was between the Allo/Al and Plg series. The formation of the side products was intensified at higher reaction temperatures e.g. for S-24 at 350°C the formation of acetaldehyde (12.0%), ethane (0.01%), methane (0.01%), carbon monoxide (0.01%), and C_3 hydrocarbons (0.01%) was detected.

The best catalytic results for dehydration of methanol and ethanol were obtained from the Allo/Ab series, and acid activation increased catalytic activity only slightly. The Plg and Sep samples were less active but acid treatment activated them very effectively for ethanol dehydration.

CONCLUSIONS

Raw allophane, palygorskite, and sepiolite samples were used as starting materials for the preparation of the catalysts for dehydration of methanol and ethanol. The first preparation

treatment was calcination of raw clays at 500°C for 6 h. The second treatment was acid activation of the raw mineral samples with a solution of nitric acid (0.8 M HNO$_3$; 95°C; 2, 8, or 24 h) followed by calcination at 500°C for 6 h. Acid treatment resulted in a significant increase in the BET surface area, pore volume, and surface concentration of acid sites for the sepiolite and palygorskite series of samples. For the allophane series, a decrease in textural parameters and surface acidity was observed after acid treatment. Among the samples studied, the best results for both methanol and ethanol dehydration were obtained from the modified allophane series, and all samples, including Plg and Sep series, performed better than γ-Al$_2$O$_3$, which is one of the commercial catalysts commonly used for these processes. The selectivity for DME and DEE was lower for the allophane-based catalyst than for γ-Al$_2$O$_3$. The high catalytic activity of these samples was related to a significant contribution of Brønsted acid sites, but, in the conversion of ethanol to ethene, Lewis base sites are postulated to also play an important role by deprotonating the intermediate ethoxide product. Palygorskite and sepiolite were significantly less catalytically active than allophane in the conversions of both methanol and ethanol; however, acid treatment resulted in a significant improvement in their catalytic performance.

ACKNOWLEDGMENTS

Compliance with Ethical Standards

Conflict of Interest
The authors declare that they have no conflict of interest.

REFERENCES

Abu-Dahrieh, J., Rooney, D., Goguet, A., & Saih, Y. (2012). Activity and deactivation studies for direct dimethyl ether synthesis using, CuO-ZnO-Al$_2$O$_3$ with NH$_4$ZSM-5, HZSM-5 or γ-Al$_2$O$_3$. *Chemical Engineering Journal, 203*, 201–211.

Alamolhoda, S., Kazemeini, M., Zaherian, A., & Zakerinasab, M. R. (2012). Reaction kinetics determination and neural networks modelling of methanol dehydration over nano γ-Al$_2$O$_3$ catalyst. *Journal of Industrial and Engineering Chemistry, 18*, 2059–2068.

Ayodele, O. B., & Abdullah, A. Z. (2019). Exploring kaolinite as dry methane reforming catalyst support: Influences of chemical activation, organic ligand functionalization and calcination temperature. *Applied Catalysis A: General, 576*, 20–31.

Bailly, M. L., Chizallet, C., Costentin, G., Krafft, J. M., Lauron-Pernot, H., & Che, M. (2005). A spectroscopy and catalysis study of the nature of active sites of MgO catalysts: Thermodynamic Brønsted basicity versus reactivity of basic sites. *Journal of Catalysis, 235*, 413–422.

Barthos, R., Szecheney, A., & Solymosi, F. (2006). Decompostion and aromatization of ethanol on ZSM-based catalysts. *Journal of Physical Chemistry: B, 110*, 21816–21825.

Batchu, R., Galvita, V. V., Alexopoulos, K., Glazneva, T. S., Poelman, H., Reyniers, M.-F., & Marin, G. B. (2019). Ethanol dehydration pathways in H-ZSM-5: Insights from temporal analysis of products. *Catalysis Today.* https://doi.org/10.1016/j.cattod.2019.04.018.

Boroń, P., Rutkowska, M., Gil, B., Marszałek, B., Chmielarz, L., & Dzwigaj, S. (2019). Experimental evidence of the mechanism of selective catalytic reduction of NO with NH$_3$ over Fe-containing BEA zeolites. *ChemSusChem, 12*, 692–705.

Bosch Reig, F., Gimeno Adelantado, J. V., & Moya Moreno, M. C. M. (2002). FTIR quantitative analysis of calcium carbonate (calcite) and silica (quartz) mixtures using the constant ratio method. Application to geological samples. *Talanta, 58*, 811–821.

Chmielarz, L., Kuśtrowski, P., Zbroja, M., Gil-Knap, B., Datka, J., & Dziembaj, R. (2004). SCR of NO by NH$_3$ on alumina or titania pillared montmorillonite modified with Cu or Co: Part II. Temperature programmed studies. *Applied Catalysis B: Environmental, 53*, 47–61.

Chmielarz, L., Kuśtrowski, P., Dziembaj, R., Cool, P., & Vansant, E. F. (2010). SBA-15 mesoporous silica modified with metal oxides by MDD method in the role of DeNOx catalysts. *Microporous and Mesoporous Materials, 127*, 133–141.

Chmielarz, L., Piwowarska, Z., Kuśtrowski, P., Wegrzyn, A., Gil, B., Kowalczyk, A., Dudek, B., Dziembaj, R., & Michalik, M. (2011). Comparison study of titania pillared interlayered clays and porous clay heterostructures modified with copper and iron as catalysts of the DeNOx process. *Applied Clay Science, 53*, 164–173.

Chmielarz, L., Wojciechowska, M., Rutkowska, M., Adamski, A., W grzyn, A., Kowalczyk, A., Dudek, B., Boroń, P., Michalik, M., & Matusiewicz, A. (2012). Acid-activated vermiculites as catalysts of the DeNOx process. *Catalysis Today, 191*, 25–31.

Chmielarz, L., Kowalczyk, A., Skoczek, M., Rutkowska, M., Gil, B., Natkański, P., Radko, M., Motak, M., Dębek, R., & Ryczkowski, J. (2018). Porous clay heterostructures intercalated with multicomponent pillars as catalysts for dehydration of alcohols. *Applied Clay Science, 160*, 116–125.

Ciftci, A., Varisli, D., Tokay, K. C., Sezgi, N. A., & Dogu, T. (2012). Dimethyl ether, diethyl ether and ethylene from alcohols over tungstophosphoric acid based mesoporous catalysts. *Chemical Engineering Journal, 207–208*, 85–93.

Colomban, P. (1989). Structure of oxide gels and glasses by infrared and Rarnan scattering. *Journal of Materials Science, 24*, 3002–3020.

Diep, B. T., & Wainwright, M. S. (1987). Thermodynamic equilibrium constants for the methanol-dimethyl ether-water system. *Journal of Chemical and Engineering Data, 32*, 330–333.

dos Santos Soares, D., Fernandes, C. S., da Costa, A. C. S., Raffi, F. N., Acchar, W., & de Lima e Moura, T. F. A. (2013). Characterization of palygorskite clay from Piauí, Brazil and its potential use as excipient for solid dosage forms containing anti-tuberculosis drugs. *Journal of Thermal Analysis and Calorimetry, 113*, 551–558.

Du, P., Yuan, P., Liu, D., Wang, S., Song, H., & Guo, H. (2018). Calcination-induced changes in structure, morphology, and porosity of allophane. *Applied Clay Science, 158*, 211–218.

Effenberger, H., Mereiter, K., & Zemann, J. (1981). Crystal structure refinements of magnesite, calcite, rhodochrosite, siderite, smithonite, and dolomite, with discussion of some aspects of the stereochemistry of calcite type carbonates. *Zeitschrift für Kristallographie – New Crystal Structures, 156*, 233–243.

Frost, R. L., Cash, G. A., & Kloprogge, J. T. (1998). 'Rocky Mountain leather', sepiolite and attapulgite – an infrared emission spectroscopic study. *Vibrational Spectroscopy, 16*, 173–184.

Frost, R. L., Kristóf, J., & Horváth, E. (2009). Controlled rate thermal analysis of sepiolite. *Journal of Thermal Analysis and Calorimetry, 98*, 423–428.

Galarneau, A., Barodawalla, A., & Pinnavaia, T. J. (1995). Porous clay heterostructures formed by gallery-templated synthesis. *Nature, 374*, 529–531.

Gil, B., Makowski, W., Marszalek, B., Roth, W. J., Kubu, M., Čejka, J., & Olejniczak, Z. (2014). High acidity unilamellar zeolite MCM-56

and its pillared and delaminated derivatives. *Journal of the Chemical Society, Dalton Transactions, 43*, 10501–10511.

Ikuta, D., Kawame, N., Banno, S., Hirajima, T., Ito, K., Rakovan, J. F., Downs, R. T., & Tamada, O. (2007). First in situ X-ray identification of coesite and retrograde quartz on a glass thin section of an ultrahigh-pressure metamorphic rock and their crystal structure details. *American Mineralogist, 92*, 57–63.

Kaufhold, S., Dohrmann, R., Abidin, Z., Henmi, T., Matsue, N., Eichinger, L., Kaufhold, A., & Jahn, R. (2010). Allophane compared with other sorbent minerals for the removal of fluoride from water with particular focus on a mineable Ecuadorian allophane. *Applied Clay Science, 50*, 25–33.

Kitagawa, Y. (1974). Dehydration of allophane and its structural formula. *American Mineralogist, 59*, 1094–1098.

Kito-Borsa, T., Pacas, D. A., Selim, S., & Cowley, S. W. (1998). Properties of an ethanol-diethyl ether-water fuel mixture for cold-start assistance of an ethanol-fueled vehicle. *Industrial and Engineering Chemistry Research, 37*, 3366–3374.

Kondo, J. N., Ito, K., Yoda, E., Wakabayashi, F., & Domen, K. (2005). An etoxy intermediate in ethanol dehydation on Bronsted acid sites in zeolite. *Journal of Physical Chemistry B, 109*, 10969–10972.

Kowalczyk, A., Borcuch, A., Michalik, M., Rutkowska, M., Gil, B., Sojka, Z., Indyka, P., & Chmielarz, L. (2017). MCM-41 modified with transition metals by template ion-exchange method as catalysts for selective catalytic oxidation of ammonia to dinitrogen. *Microporous and Mesoporous Materials, 240*, 9–21.

Li, B., Li, L., Zhang, Q., Weng, W., & Wan, H. (2017). Attapulgite as natural catalyst for glucose isomerization to fructose in water. *Catalysis Communications, 99*, 20–24.

Liu, L., Chen, H., Shiko, E., Fan, X., Zhou, Y., Zhang, G., Luo, X., & Hu, X. (2018a). Low-cost DETA impregnation of acid-activated sepiolite for CO_2 capture. *Chemical Engineering Journal, 353*, 940–948.

Liu, R., Ji, Z., Wang, J., & Zhang, J. (2018b). Solvothermal synthesized Ag-decorated TiO_2/sepiolite composite with enhanced UV-vis and visible light photocatalytic activity. *Microporous and Mesoporous Materials, 266*, 268–275.

Macina, D., Piwowarska, Z., Tarach, K., Góra-Marek, K., Ryczkowski, J., & Chmielarz, L. (2016). Mesoporous silica materials modified with alumina polycations as catalysts for the synthesis of dimethyl ether from methanol. *Materials Research Bulletin, 74*, 425–435.

Madejová, J., & Komadel, P. (2001). Baseline studies of the Clay Minerals Society source clays: infrared methods. *Clays and Clay Minerals, 49*, 410–432.

Madarász, J., Varga, P. P., & Pokol, G. (2007). Evolved gas analyses (TG/DTA–MS and TG–FTIR) on dehydration and pyrolysis of magnesium nitrate hexahydrate in air and nitrogen. *Journal of Analytical and Applied Pyrolysis, 79*, 475–478.

Marosz, M., Kowalczyk, A., & Chmielarz, L. (2019). Modified vermiculites as effective catalysts for dehydration of methanol and ethanol. *Catalysis Today*. https://doi.org/10.1016/j.cattod.2019.07.003.

Mironyuk, I., Mandzyuk, V., Sachko, V. M., & Gun'ko, V. (2016). Structural and morphological features of disperse alumina synthesized using aluminum nitrate nonahydrate. *Nanoscale Research Letters, 11*, 153.

Mnasri-Ghnimi, S., & Frini-Srasra, N. (2019). Removal of heavy metals from aqueous solutions by adsorption using single and mixed pillared clays. *Applied Clay Science, 179*, 105151.

Opiso, E., Sato, T., & Yoneda, T. (2009). Adsorption and co-precipitation behavior of arsenate, chromate, selenate and boric acid with synthetic allophane-like materials. *Journal of Hazardous Materials, 170*, 79–86.

Papoulis, D., Komarneni, S., Nikolopoulou, A., Tsolis-Katagas, P., Panagiotaras, D., Kacandes, H. G., Zhang, P., Yin, S., Sato, T., & Katsuki, H. (2010). Palygorskite- and Halloysite-TiO_2 nanocomposites: Synthesis and photocatalytic activity. *Applied Clay Science, 50*, 118–124.

Pérez, N. A., Bucio, L., Lima, E., Soto, E., & Cedillo, C. (2016). Identification of allophane and other semi-crystalline and amorphous phases on pre-Hispanic Mexican adobe earth bricks from Cholula, Mexico. *Microchemical Journal, 126*, 349–358.

Perraki, T., & Orfanoudaki, A. (2008). Study of raw and thermally treated sepiolite from the Mantoudi Area, Euboea, Greece. *Journal of Thermal Analysis and Calorimetry, 91*, 589–593.

Pluth, J. J., Smith, J. V., & Faber, J. (1985). Crystal structure of low cristobalite at 10, 293, and 473 K: Variation of framework geometry with temperature. *Journal of Applied Physics, 57*, 1045–1049.

Rampe, E. B., Kraft, M. D., Sharp, T. G., Golden, D. C., Ming, D. W., & Christensen, P. R. (2012). Allophane detection on Mars with thermal emission spectrometer data and implications for regional-scale chemical weathering processes. *Geology, 40*, 995–998.

Rastsvetaeva, R. K., Chukanov, N. V., & Zadov, A. E. (2009). Refined structure of afwillite from the northern Baikal region. *Crystallography Reports, 54*, 418–422.

Rodriguez-Blanco, J. D., Shaw, S., & Benning, L. G. (2011). The kinetics and mechanisms of amorphous calcium carbonate (ACC) crystallization to calcite, via vaterite. *Nanoscale, 3*, 265–271.

Rownaghi, A. A., Rezaei, F., Stante, M., & Hedlund, J. (2012). Selective dehydration of methanol to dimethyl ether on ZSM-5 nanocrystals. *Applied Catalysis B: Environmental, 119–120*, 56–61.

Sing, K. S. W., & Williams, R. T. (2004). The use of molecular probes for the characterization of nanoporous adsorbents. *Particle and Particle Systems Characterization, 21*, 71–79.

Sing, K. S. W., Everett, D. H., Haul, R. A. W., Moscou, L., Pierotti, R. A., Rouquérol, J., & Siemieniewska, T. (1985). Reporting physisorption data for gas/solid systens with special reference to the determination of surface area and porosity. *Pure and Applied Chemistry, 57*, 603–619.

Srinivasan, P. D., Khivantsev, K., Tengco, J. M. M., Zhu, H., & Bravo-Suárez, J. J. (2019). Enhanced ethanol dehydration on γ-Al_2O_3 supported cobalt catalyst. *Journal of Catalysis, 373*, 276–296.

Stiefel, M., Ahmad, R., Arnold, U., & Döring, M. (2011). Direct synthesis of dimethyl ether from carbon-monoxide-rich synthesis gas: Influence of dehydration catalysts and operating conditions. *Fuel Processing Technology, 92*, 1466–1474.

Takahara, A., Saito, M., Inaba, M., & Murata, K. (2015). Dehydration of ethanol into ethylene over solid acid catalysts. *Catalysis Letters, 105*, 249–252.

Thill, A. (2016). Characterisation of imogolite by microscopic and spectroscopic methods. Pp. 223–253 in: *Nanosized Tubular Clay Minerals Halloysite and Imogolite* (P. Yuan, A. Thill, & F. Bergaya, editors). *Developments in Clay Science*, vol. 7. Elsevier, Amsterdam.

Thommes, M., Kaneko, K., Neimark, A. V., Olivier, J. P., Rodriguez-Reinoso, F., Rouquerol, J., & Sing, K. S. W. (2015). Physisorption of gases, with special reference to the evaluation of surface area and pore size distribution (IUPAC Technical Report). *Pure and Applied Chemistry, 87*, 1051–1069.

Tian, Y., Yang, J., Yang, C., Lin, F., Hu, G., Kong, M., & Liu, Q. (2019). Comparative study of the poisoning effect of NaCl and Na_2O on selective catalytic reduction of NO with NH_3 over V_2O_5-WO_3/TiO_2 catalyst. *Journal of the Energy Institute, 92*, 1045–1052.

Tokay, K. C., Dogu, T., & Dogu, G. (2012). Methanol dehydration reaction to produce clean diesel alternative dimethyl ether over mesoporous aluminosilicate-based catalysts. *Chemical Engineering Journal, 184*, 278–285.

Ue, M., Mizutani, F., Takeuchi, S., & Sato, M. (1997). Characterization of anodic films on aluminum formed in carboxylate-based nonaqueous electrolyte solutions. *Journal of the Electrochemical Society, 144*, 3743–3748.

Varisli, D., Dogu, T., & Dogu, G. (2007). Ethylene and diethyl-ether production by dehydration reaction of ethanol over different heteropoly acid catalysts. *Chemical Engineering Science, 62*, 5349–5352.

Vicente-Rodriguez, M. A., Suarez, M., Bañares-Muñoz, M. A., & Lopez-Gonzalez, J. D. (1996). Comparative FT-IR study of the removal and structural modifications during acid silicates. *Spectrochimica Acta A, 52*, 1685–1694.

Vinoda, B. M., Vinuth, M., Bodke, Y. D., & Manjanna, J. (2015). Photocatalytic degradation of toxic methyl red dye using silica nanoparticles synthesized from rice husk ash. *Journal of Environmental and Analytical Toxicology, 05*, 336.

Xu, L., Penga, T., Tiana, J., Lua, Z., Hu, Y., & Sun, W. (2017). Anisotropic surface physicochemical properties of spodumene and albite crystals: Implications for flotation separation. *Applied Surface Science, 426*, 1005–1022.

Yaripour, F., Baghaei, F., Schmidt, I., & Perregaard, J. (2005). Catalytic dehydration of methanol to dimethyl ether (DME). over solid-acid catalysts. *Catalysis Communications, 6*, 147–152.

Zheng, J., Zeng, Q., Yia, Y., Wang, Y., Ma, J., Qin, B., Zhang, X., Sun, W., & Li, L. (2011). The hierarchical effects of zeolite composites in catalysis. *Catalysis Today, 168*, 124–132.